HHS Public Access

Author manuscript

FASEB J. Author manuscript; available in PMC 2021 August 01.

Published in final edited form as:

FASEB J. 2020 October ; 34(10): 13792–13808. doi:10.1096/fj.202001191R.

Deficiency in Acyl-CoA:Wax Alcohol Acyltransferase 2 causes evaporative dry eye disease by abolishing biosynthesis of wax esters

Made Airanthi K. Widjaja-Adhi[1], **Josie A. Silvaroli**[1], **Sylwia Chelstowska**[1], **Thomas Trischman**[1], **Ilya Bederman**[2], **Rony Sayegh**[3], **Marcin Golczak**[1,4]

[1]Department of Pharmacology, School of Medicine, Case Western Reserve University, Cleveland, OH, USA

[2]Department of Genetics and Genome Sciences, School of Medicine, Case Western Reserve University, Cleveland, OH, USA

[3]Department of Ophthalmology, School of Medicine, Case Western Reserve University, Cleveland, OH, USA

[4]Cleveland Center for Membrane and Structural Biology, School of Medicine, Case Western Reserve University, Cleveland, OH, USA

Abstract

Lipids secreted by the meibomian glands (MGs) of the eyelids are essential to the protection of the eye's surface. An altered meibum composition represents the primary cause of evaporative dry eye disease (DED). Despite the critical importance of the meibum, its biosynthetic pathways and the roles of individual lipid components remain understudied. Here, we report that the genetic deletion of Acyl-CoA:wax alcohol acyltransferase 2 (AWAT2) causes the obstruction of MGs and symptoms of evaporative DED in mice. The lipid composition of the meibum isolated from *Awat2*$^{-/-}$ mice revealed the absence of wax esters, which was accompanied by a compensatory overproduction of cholesteryl esters. The resulting increased viscosity of meibum led to the dilation of the meibomian ducts, and the progressive degeneration of the MGs. Overall, we provide evidence for the main physiological role of AWAT2 and establish *Awat2*$^{-/-}$ mice as a model for DED syndrome that can be used in studies on tear film-oriented therapies.

Correspondence: Marcin Golczak and Made Airanthi K. Widjaja-Adhi, Department of Pharmacology, School of Medicine, Case Western Reserve University, 10900 Euclid Ave, Cleveland, OH 44106, USA. mxg149@case.edu (M. G.) and nkw5@case.edu (M. A. K. W.-A.).

AUTHOR CONTRIBUTIONS

M.A.K. Widjaja-Adhi, T. Trischman, R. Sayegh, and M. Golczak contributed to the design of the experiments, discussed research plans and data. M.A.K. Widjaja-Adhi, J.A. Silvaroli, S. Chelstowska, T. Trischman, I. Bederman, R. Sayegh, and M. Golczak carried out the experiments. M.A.K. Widjaja-Adhi and M. Golczak wrote the first and edited subsequent drafts of the manuscript. J.A. Silvaroli, S. Chelstowska, T. Trischman, I. Bederman, and R. Sayegh edited subsequent drafts of the manuscript.

CONFLICT OF INTEREST

The authors declare that they have no competing interests.

SUPPORTING INFORMATION

Additional supporting information may be found online in the Supporting Information section.

Keywords

AWAT2; dry eye disease; MFAT; tear film; wax esters

1 | INTRODUCTION

The ocular surface is continuously challenged by the shearing forces of the external environment. To preserve the health of the eyes, the front of the cornea is covered by a protective tear film. It is comprised of three layers: mucous, aqueous tears, and the outermost portion called the tear-film lipid layer.[1] The lipids that spread over the tears after each blink reduce the evaporation of the aqueous phase, maintain tear-film stability, and provide lubrication that smoothens the movement of the eyeball and eyelids.[2,3] The lipids of the tear film are secreted by the meibomian glands (MGs).[4,5] These specialized structures are formed by multiple holocrine secretory acini embedded within the tarsal plate along the rims of the upper and lower eyelids.[5,6] The discharge from the MGs (called meibum) is a complex mixture of lipids, many of which are synthetized exclusively by these glands.[7] The main components of the meibum include non-polar cholesteryl esters, esterified long-chain alcohols (wax esters), and triacylglycerols. Less abundant components include (O)-acylated ω-hydroxy fatty acids and their esters, as well as diacylated fatty α,ω-diols (wax diesters).[8,9]

A deficiency in the proper formation of the tear film plays a key role in the development of dry eye disease (DED). This common and persistent ocular surface condition affects tens of millions of people worldwide, impacting their quality of life by causing acute and chronic symptoms that lead to secondary changes in the ocular surface and impair vision.[10–13] Although DED is a multifactorial syndrome, the majority of patients affected by DED reveal signs of abnormalities in the chemical composition or an impaired secretion of the tear film lipids that contribute to the evaporative form of DED.[14,15] However, despite their clinical significance, the enzymatic processes involved in the production of the meibum and the roles of the individual lipid components of the tear film remain largely under-investigated, hindering the development of effective therapeutic strategies against evaporative DED.

Several lines of evidence indicate that meibum lipids are synthetized de novo in the MGs.[16,17] Importantly, the uniqueness of meibum lipid composition indicates the presence of specialized metabolic pathways not found in other cell types.[9,18] The transcriptome analysis of MGs isolated from mice indicated that among ubiquitous proteins commonly associated with lipid biosynthesis there are several enzymes preferentially expressed in the meibomian and sebaceous glands.[7] One of them is acyl-CoA:wax alcohol acyltransferases 2 (AWAT2). This representative of the DGAT2 protein family reveals broad substrate specificity when examined in vitro. In addition to the formation of wax esters, AWAT2 facilitates the transfer of acyl moieties onto mono- and diacylglycerols to yield triacylglycerols or all-*trans*-retinol and its geometric isomers to produce corresponding retinyl esters.[19–22] Therefore, AWAT2 is also referred to as multifunctional fatty acid transferase (MFAT).[19] Its substrate specificity and tissue distribution implicate AWAT2 in wax ester synthesis, although this or any other function of this enzyme has not yet been verified in vivo.

To reconcile the functional significance of this enzyme in the biosynthesis of lipids, we generated *Awat2* knockout mice (*Awat2*$^{-/-}$) and examined the phenotypic consequences of the ablation of AWAT2 enzymatic activity. Our data identify AWAT2 as a non-redundant enzyme responsible for wax ester production in MGs. Its absence alters the lipid composition of meibum preventing efficient lipid secretion to the ocular surface and tear film lipid layer formation. Consequently, *Awat2*$^{-/-}$ mice suffer from evaporative DED that progresses into alterations of the ocular surface and the gradual degeneration of the meibomian glands. The phenotype of AWAT2-deficient mice makes them a valuable experimental model for studying the etiology of evaporative DED and evaluating methods for the treatment or prevention of this eye condition.

2 | MATERIAL AND METHODS

2.1 | Animal genetic manipulation and genotyping

The generation of the genetically modified mouse line was subcontracted to the InGenious Targeting Laboratory. The *Awat2*-knockout mice (*Awat2*$^{-/-}$) were generated by the deletion of a portion of the *Awat2* gene using the *cre/loxP* recombination system. Briefly, the final targeting vector was constructed using conventional cloning techniques and then transfected by the electroporation of HF4 (129/SvEv × C57BL/6) FLP hybrid embryonic stem cells (InGenious Targeting Laboratory). The ~1.7 kb target region containing exons 3, 4, and 5 of the *Awat2* gene was flanked by the *loxP* and *loxP*/FRT Neo cassettes (Figure 1A). The Neo cassette in the targeting vector was removed upon selection and clone expansion. The selected embryonic stem cells were microinjected into C57BL/6 blastocysts and the resulting chimeras were mated to C57BL/6 mice to generate germline Neo deleted mice Awat2-LoxP heterozygotes (*Awat2*$^{fl/+}$). The *Awat2*$^{fl/+}$ were then backcrossed to C57BL/6J, and since the Awat2 gene is located on the X chromosome, 25% of the offspring were Awat2-LoxP hemizygotes (*Awat2*$^{fl/Y}$). To generate global knockout mice (*Awat2*$^{-/-}$), *Awat2*$^{fl/Y}$ mice were crossed with female *Sox2-cre* transgenic mice (B6-CgTg(Sox2-cre)1Amc/J from The Jackson Lab (Stock# 008454) for the excision of *loxP* flanked *Awat2* gene (Figure 1A). *Sox2-cre* was inherited maternally, thus the excision occurs in all offspring irrespective of whether they carry the *cre* transgene.[23,24] The experiments described in this report were conducted with female non-carrier Sox2-cre *Awat2*$^{-/-}$ (homozygous females) and male non-carrier Sox2-cre *Awat2*$^{-/Y}$ (hemizygous males). For simplicity hereafter both sex mice were named *Awat2*$^{-/-}$ or KO and their wild type (female non-carrier Sox2-cre *Awat2*$^{+/+}$ and male non-carrier Sox2-cre *Awat2*$^{+/Y}$) littermates were assigned as WT. Genotyping was conducted by genomic PCR using the primers SC1, SDL2, and NDEL2 for the *Awat2* gene and 15495, oIMR6082, oIMR7338, oIMR7339 for Sox2-cre (Figure 1B, Table S1, and Figure S1). The levels of *Awat2* transcript were verified by real-time quantitative PCR (RT-qPCR) (Figure 1C). For genotyping and RT-qPCR evaluations DNA was isolated from the outer ear of examined mice. The absence of AWAT2 was also verified by immunofluorescence (Figure 1D).

All mice used in this study were housed in the pathogen-free animal facility at the School of Medicine, Case Western Reserve University, where they were maintained under a 12-h light/12-h dark cycle (~50 lux) environment with food and water available ad libitum. All

animal procedures and experiments were approved by the Case Western Reserve University Animal Care Committee and conformed to both the recommendations of the American Veterinary Medical Association Panel on Euthanasia and the Association of Research for Vision and Ophthalmology.

2.2 | RT-qPCR analyses

Isolated outer ear, ventral skin, liver, intestine, spleen, lung, heart, kidney, epididymal white adipose tissue, inguinal white adipose tissue, brown adipose tissue, retina, retinal pigment epithelium, brain, and muscle were stored in an RNA*later* storage solution (Sigma-Aldrich) until analyses. Total mRNA isolation was carried out with the RNeasy Mini Kit (Qiagen) according to the manufacturer's instructions. RNA concentration and purity were measured with a Nanodrop spectrophotometer (ND-1000, Thermo Scientific). The Applied Biosystems reverse transcription kit (4368814, Applied Biosystems) was used to reverse transcribe up to 2 μg (for a 20 μL reaction) of total RNA to cDNA. RT-qPCR was carried out with TaqMan probes (Applied BioSystems) for *Awat2* (Mm01232858_m1). Gapdh (Mm99999915_g1) was used as an endogenous control. All real-time experiments were performed with an ABI Step-One Plus RT-qPCR instrument (Applied BioSystems).[25] The data were normalized to GAPDH expression levels and fold changes were calculated using amplification curve analysis (StepOne software version 2.3).[25]

2.3 | Immunofluorescence staining

Mouse tarsal plate, cornea, and skin were immediately fixed in 4% formaldehyde-PBS solution. Twenty-four hours later they were placed in 30% sucrose solution in 137 mM NaCl, 2.7 mM KCl, 10 mM Na_2HPO_4, 1.8 mM KH_2PO_4 solution (PBS). After the tissues were fully saturated with sucrose, they were embedded in optimal cutting temperature compound medium (Sakura Fine Chemicals), and then frozen. Cryosections were cut using a cryostat-microtome (Leica) at 5 μm thickness. Sections were collected onto Fisher Superfrost Plus slides and allowed to dry, then stored at −20°C. For immunofluorescence staining, nine frozen sections from three different mice from each experimental condition were air-dried for 30 minutes and then washed twice in PBS for 5 minutes at room temperature. Sections were then permeabilized and blocked in 2% goat serum, 1% bovine serum albumin, and 0.1% Triton X-100 in PBS at room temperature, and shaken for 1 hour in a rocker (Rocker 25, Labnet International) at 20 rpm. Then the sections were incubated overnight at 4°C with appropriate antibody: either the rabbit anti-AWAT2 (NBP1–91574 from Novus Biologicals) antibody at 1:100 dilution, PE-conjugated rat anti-mouse CD45 (553081 from BD Biosciences) antibody at 1:50 dilution, or PE-conjugated rat IgG2b κ isotype control (553989 from BD Biosciences) antibody at a 1:50 dilution, rabbit anti-LYVE1 (ab14917 from Abcam) antibody at a 1:50 dilution, or rabbit anti-cytokeratin 6a (NBP1–3443 from Novus Biologicals) antibody at 1:50 dilution. For the rabbit anti-cytokeratin 6a, immunofluorescence was performed on a paraffin-section. Next, the sections were washed three times with PBS for 10 minutes and incubated with a 1:400 dilution of the secondary antibody, Alexa Fluor 555 conjugated goat anti-rabbit IgG or Alexa Fluor 488 conjugated goat anti-rabbit IgG (Life Technologies) in the blocking buffer. Finally, the sections were washed three times for 15 minutes each with PBS, mounted in mounting medium (Prolong Gold Antifade Reagent containing 4′,6-diamidino-2-phenylindole,

Intrivogen), and covered with cover glass and allowed to dry. Fluorescent images were obtained either on a Leica 6000b inverted microscope using a 20× objective connected to an ExiAqua Blue camera (Teledyne QImaging) and MetaMorph Imaging software (Molecular Devices) or Olympus FV1200 Laser Scanning Microscope using laser diode 405nm, 50mW for DAPI, 473 nm, 15 mW for Alexa Fluor 488, or 559 nm, 20 mW for PE with a 10× or 20× objective on Olympus IX83 inverted microscope.

2.4 | Slit-lamp biomicroscopy

To examine the ocular surface, mice were anesthetized with a ketamine/xylazine cocktail and evaluated using a slit lamp bio-microscope (SL-5000, Hai Laboratories). Each mouse was placed in an animal holder in the light path of the slit lamp and the ocular surface and eyelids were observed and real-time images were captured using an attached 3CCD camera (Hitachi HV-D30, Hitachi Kokusai) and HAI IMS/CL 8.0 image management system.

2.5 | Phenol Red Thread (PRT) test

The PRT test measures the residual tear film in the inferior conjunctival sac of the eye.[26] Phenol red thread (ZONE-QUICK) is yellow in color (acidic) and when it comes in contact with tears it changes in a light red color (basic). The mice were anesthetized with a ketamine/xylazine cocktail before the PRT test. Forceps were used to insert the 3 mm folded portion of the thread into the palpebral conjunctiva of the eye 1/3 of the distance from the lateral canthus of the lower eyelid. After 15 seconds, the thread was removed and measured according to the scale provided by the manufacturer; measurements were based on post-experimental photograph analysis of the PRTs using ImageJ to maximize accuracy.

2.6 | Tear Film Break Up Time (TFBUT) test

To examine the stability of the tear film, the anesthetized mice were placed on the slit lamp bio-microscope and sodium fluorescein staining was performed by the administration of 1 μL of 0.1% fluorescein-dye solution and visualized under a broad beam of cobalt blue illumination. The cobalt-blue filter produces blue light in which fluorescein dye fluoresces with a yellow-green color. Prior to testing, the residual tear film in the inferior conjunctival sac was removed for a standard time (15 seconds). The TFBUT test was conducted one minute after the removal of the residual tears in the inferior conjunctival sac.

2.7 | Spectral Domain Optical Coherence Tomography (SDOCT)

To further evaluate ocular structures that may not be easy to evaluate using slit-lamp bio-microscopy alone, the mouse eye anterior segment was examined by SDOCT (Envisu R2210, Bioptigen). Anterior segment-OCT provides real-time imaging and the ability to record changes in ocular structures with age. The mice were anesthetized with a ketamine/xylazine cocktail before imaging. The morphology and integrity of the ocular surface and tear film, corneal thickness, as well as anterior chamber structures, and the meibomian glands were examined using Envisu application software.

2.8 | Hematoxylin and eosin staining

The structural morphology of mouse meibomian glands, corneas, irises, and retinas was assessed using Hematoxylin and Eosin (H&E) staining of paraffin sections. Mouse eyes and eyelids were fixed in 4% paraformaldehyde and 1% glutaraldehyde followed by paraffin sectioning. Fixed tissues were washed with PBS and processed through a Sakura Tissue-Tek VIP E-300 vacuum infiltration paraffin processor. Briefly, tissues were placed in 70% ethanol then dehydrated by increasing concentrations of ethanol (70% for 40 minutes, 80% for 40 minutes, and 95% for 40 minutes, and 100% for 45 minutes). The ethanol was exchanged with xylene by a repeated incubation for 1 hour. To exchange xylene with paraffin, the samples were incubated in melted paraffin for 30 minutes. This procedure was repeated four times. The tissues were then kept in melted paraffin until they were embedded in fresh paraffin using the Tissue-Tek paraffin embedding center. Sections were sliced in 5μm thickness on a Microm HM355 paraffin microtome and affixed onto microscopic slides. Paraffin sections were stained with H&E and imaged using a high-resolution bright-field light microscope (Leica) connected to an Exi Aqua Blue camera (Teledyne QImaging) equipped with a 20× objective. Metamorph Imaging software (Molecular Devices) with a scan slide module was employed for acquisition of multiple images and stiches them together for full tissue samples image reconstruction.

2.9 | Oil Red O staining

Oil Red O staining of frozen sections was carried out with the Oil Red O Stain Kit (KTORO from American MasterTech Scientific) according to manufacturer's instructions and images using a high-resolution bright-field light microscope (Leica 6000b inverted microscope) with a 20× objective.

2.10 | Collection of mouse meibum

To collect meibum samples, mice were anesthetized with a ketamine/xylazine cocktail and placed in the light path of a slit-lamp bio-microscope to directly visualize meibum secretion from the MG orifices. After gently squeezing the mouse eyelid, the MG discharge was carefully collected from the upper and lower eyelids using a stainless-steel micro spatula, and tears were collected from the lower menisci using microcapillaries, and transferred to glass test tubes that contained 1 mL of hexane. The samples were dried under a stream of nitrogen to remove the organic solvent and traces of water, re-dissolved in 1 mL of hexane, placed in new glass vials sealed with crimped Teflon-lined caps, and stored in −80°C until analysis. Meibum samples were obtained from five mice for each experimental group by the gentle squeezing of the eyelids three times with 2-minutes intervals. To obtain enough samples, the meibum collection sessions were repeated after a day of recovery.

2.11 | Analysis of the lipid composition of meibum

Liquid chromatography-mass spectrometry (LC-MS)-base detection and the identification of the lipid components of the meibum was performed using an LTQ linear ion trap mass spectrometer (Thermo Scientific) in line with an Agilent 1100 series HPLC system (Agilent Technologies) and equipped with an atmospheric pressure chemical ionization (APCI) source working in positive mode. The meibum lipids were separated on a normal phase Luna

Silica column (250 × 4.6 mm, 10 μm) (Phenomenex) in a linear gradient of ethyl acetate in hexane (1% to 10%, v/v) developed over 15 minutes and followed by an isocratic flow of 10% (v/v) ethyl acetate in hexane for another 15 minutes at the flow rate of 1 mL/min. The quantification of cholesteryl esters and wax esters was achieved based on the relationship between areas under ion intensity peaks corresponding to endogenous lipids and the amount of internal standards, deuterated cholesteryl-d7 palmitate (Avanti Polar Lipids) and Myristyl palmitate (Toronto Research Chemicals), respectively.

To determine the fatty acid (FA) composition of the meibum, 1 mL of lipid samples in hexane were hydrolyzed in 0.2 mL of 2 N NaOH, vortexed, and incubated at 80°C for 30 minutes. The hydrolysis was quenched by lowering the pH with 0.2 mL of 2 M HCl. The mixture was separated by centrifugation at 3000 rpm for 5 minutes. The upper hexane layer containing the FAs was recovered, evaporated in a stream of nitrogen, and the residual lipids were redissolved in 1:1 ethanol:isopropanol (v/v) solution, containing 0.1% formic acid (v/v). The FAs were separated on a Hypersil Gold (50 × 2.1 mm) reverse phase HPLC column (Thermo Scientific) in a linear gradient 50%−100% of mobile phase A (water) and B (1:1 acetonitrile:isopropanol) developed over 10 minutes and followed by an isocratic flow of solvent B for an additional 5 minutes. Both solvents A and B contained 10 mM ammonium acetate. The flow rate was set at 0.3 mL/min. The eluent was directed into an LTQ linear ion trap mass spectrometer (Thermo Scientific) via an electrospray ionization probe working in the negative mode. To ensure adequate sensitivity, the mass spectrometer parameters were tuned for pentacosanoic acid (Cayman Chemicals). Areas under ion intensity peaks were used to estimate the percentage contribution of detected FAs in the mixture.

2.12 | Statistical analyses

Results are presented as boxplot-and whiskers graphs. The boxes represent standard deviation values, the mean is marked by a vertical line inside the box, whereas the whiskers correspond to min and max values. The number of samples and independent experiments are indicated in the figure legends. Statistical significance was assessed using one-way analysis of variance (ANOVA) followed by the Scheffe test using Origin 9 software (OriginLab Corporation), with the threshold of significance set at $^{*}P < .001$.

3 | RESULTS

3.1 | Targeting of the *Awat2* gene and generation of AWAT2-deficient mice

To study the role of AWAT2 in vivo, we generated a genetically modified mouse with an inactivated *Awat2* gene. Because genetic intervention in lipid metabolism is often correlated with neonatal or postnatal mortality and morbidity, we decided to create a construct in which exons 3–5 of the *Awat2* gene were flanked by LoxP sites (Figure 1A). This design allowed us to produce global or tissue-specific knockout mouse lines, and thus avoid potential problems with the premature mortality of the knockout mice. To ensure the complete inactivation of AWAT2, the excision of these exons eliminated the part of the enzyme containing the catalytic residues ^{107}HPHG^{110} encoded in exon 3[27] and introduced a stop codon disabling the transcription of the following exons 6 and 7.

To generate the global *Awat2* knockout mouse model ($Awat2^{-/-}$) through the deletion of the floxed target gene, the male $Awat2^{fl/Y}$ mice were crossbred with the female *Sox2-cre* transgenic mice (B6-Cg-Tg(Sox2-cre)1Amc/J from The Jackson Laboratories).[28] These transgenic mice express *Cre* recombinase which is active in the female germline, and deletes the floxed sequences of the *Awat2* gene, resulting in female *Awat2* heterozygous mice ($Awat2^{+/-}$) and male *Awat2* wild type mice littermates ($Awat2^{+/Y}$). The female *Awat2* heterozygous mice ($Awat2^{+/-}$) that carry the *Sox2*-cre gene were then backcrossed to male $Awat2^{fl/Y}$ mice to generate female *Awat2* homozygous mice ($Awat2^{-/-}$) and male *Awat2* hemizygous mice ($Awat2^{-/Y}$). The genotypes were confirmed by PCR using SC1/SDL2 (475 bp) and SC1/NDEL2 (387 bp) primer pairs for the wild-type (WT) and Cre-excised *Awat2* gene, respectively (Figure 1B). The final $Awat2^{-/-}$ mouse line did not carry the *Sox2*-cre gene (Figure S1). The lack of expression of AWAT2 was verified by comparing the relative levels of *Awat2* transcript in WT, heterozygotes, and homozygotes of female mice by RT-qPCR (Figure 1C). Also, the immunocytochemistry staining of skin and tarsal plate sections isolated from $Awat2^{-/-}$ animals revealed the absence of the enzyme in the sebaceous and meibomian glands (Figure 1D). Importantly, $Awat2^{-/-}$ mice developed normally, were vital, and indistinguishable from their WT siblings at birth.

3.2 | MG dysfunction causes dry eye phenotype in AWAT2-deficient mice

Phenotypic differences between the WT and $Awat2^{-/-}$ mice became noticeable immediately after eye-opening (Figure 2A). Although we did not observe any significant delay in the eye-opening process, which occurred at about 10 to 12 days postnatal, the eyes of $Awat2^{-/-}$ mice remained partially covered by the eyelids, giving them a narrower, slit-like look distinctive from wide-open eyes of the WT littermates. This difference in eye appearance was confirmed by quantitative measurements of the ratio between the horizontal and vertical dimensions of the eye slits opening (Figure 2B). Importantly, there were no changes in the overall size of the eyeball as calculated by adding central corneal thickness, anterior chamber depth, vitreous chamber depth, and retina thickness in the OCT image. (Figure 2C) There were also no other early morphological abnormalities that could indicate developmental deficiencies affecting $Awat2^{-/-}$ mice. Above all, the phenotypic hallmark that distinguished $Awat2^{-/-}$ mice from their WT littermates was the white discharge present around the superior and inferior lid margins (Figure 2D-G). This soft material originated from well-defined locations on the eyelids that appeared to represent the orifices of the MGs (Figure 2F,G). Indeed, in contrast with the WT mice, the slit-lamp examination of the lid tarsal plates of $Awat2^{-/-}$ mice revealed long white marks at the palpebral conjunctiva accompanied by telangiectasia (Figure 2D,F). This long white shape appears to be the MG central duct loaded with a large amount of accumulated toothpaste-like material. It could be squeezed out by applying gentle pressure to the lid margins. However, its high density did not allow for spontaneous outflow from the MG orifices, causing MG central duct plugging clearly seen in the OCT images (Figure 2H,I). The ocular phenotype was bilateral and started to be macroscopically evident in the second month of life for all examined AWAT2-deficient mice. It was also observed for both males and females lacking the enzyme (Figure S2A).

The difficulties in meibum secretion in *Awat2*$^{-/-}$ mice most likely contribute to the suboptimal formation of the tear film that, in turn, caused the early phenotypic consequence similar to obstructive dry eye disease related to MG dysfunction. This assumption is further supported by the instability of the tear film of *Awat2*$^{-/-}$ mice, which showed significantly shorter tear film break-up time (TFBUT) compared to the WT mice (Figure 2J). Furthermore, the knockout mice retained residual tear film in the inferior conjunctival sac of the eye as visualized by slit-lamp bio-microscopy and measured by the length of phenol red threads (Figure 2H). A nonstandard behavior of *Awat2*$^{-/-}$ mice was also observed where an extensive wiping of the eyes and front of the head, repetitive scratching of cheeks and ears as well as restlessness, which was most likely related to chronic itching and gritting sensations.

These macroscopic observations of the phenotype were further evaluated by assessing histopathological changes in the MGs. Histology sections of tarsal plates isolated from 2-month old males and females of *Awat2*$^{-/-}$ mice showed dramatically dilated central ducts, disproportional to their narrow orifices when compared to tarsal plates isolated from WT mice (Figure 3A-E and Figure S2B,C). Despite this abnormality, regularly arranged cells in the basal parts of the acini and the presence of meibocytes in different stages of differentiation indicated that initially the maturation and lipid secretion function of the glands were intact in *Awat2*$^{-/-}$ mice. However, the persistent obstruction of the orifice and excretory duct in association with the hyperkeratinization of the epithelium (Figure 3C,D) and the continuous secretion of lipids in the acini led to the progressive degeneration of MGs. The secretory acini became distinctly smaller compared to WT mice as evident by a decreased number of meibocytes (Figure 3F,G). The ductal epithelium became highly cornified and the central duct filled with accumulated eosinophilic material that most likely represents the protein component of cellular keratin debris (Figure 3B,D).

3.3 | AWAT2-deficiency abolishes the biosynthesis of wax esters in the MGs

To elucidate the underlying cause of the ocular abnormalities caused by AWAT2 deficiency, we examined the lipid composition of meibum collected from WT and *Awat2*$^{-/-}$ mice. We choose mature 4-month old mice to capture changes in meibum lipids before significant degeneration of the MGs occurred. Consistent with the previous reports, LC-MS analysis of the hexanoic extracts of WT mouse meibum revealed the presence of two major classes of lipids, cholesteryl esters (detected as m/z 369.3 ion $[M + H - FA - H_2O]^+$) and wax esters (m/z range 591.7–757.7) with the characteristic distribution of lengths the carbon chains.[9,29,30] Minor lipid components were triacylglycerides (m/z from 831.9 to 1026.1 $[M + H]^+$) and unesterified cholesterol (m/z = 369.3 $[M + H - H_2O]^+$) (Figure 4A-F and Figure S3). Notably, a direct comparison of the meibum lipid profile between the WT and *Awat2*$^{-/-}$ mice revealed striking qualitative and quantitative differences. The most profound change was a >95% reduction in the amount of wax ester species (Figure 4C,G). Based on internal standard quantification, the amount of wax esters in WT mice was calculated to be 294.9 ± 32.9 pmols per 1 μg of meibum. This value decreased to 14.4 ± 7.4 pmol/μg in meibum isolated from AWAT2-deficient mice. This profound decrease equally affected all species of wax esters, regardless of their acyl chain lengths or the level of saturation. Thus, AWAT2 is responsible for the biosynthesis of the entire class of neutral lipids. Remarkably, the missing volume of wax esters was largely compensated by an increase in the concentration of

cholesteryl esters. Their amount increased nearly 6-fold from 25.6 ± 5.6 pmol/μg in WT meibum to 149.7 ± 32.9 pmol/μg in *Awat2*$^{-/-}$ mice (Figure 4B,G). Consistently with the phenotypic similarities between the sexes, this abnormal meibum composition was detected in male and female AWAT2-deficient mice (Figure S2D,E). Additionally, the samples obtained from the knockout mice revealed elevated levels of wax diesters, a class of lipids that were not readily detectable in our experimental system in the control mice (Figure 4E). Molecular masses within the wax diester population range between 845.8 and 1026.1 Da that correspond to compounds with total acyl chain lengths between 56 and 66 carbons (Figure S4). The majority of detected wax diesters contained one or two unsaturated C=C bonds. Additionally, the meibum from *Awat2*$^{-/-}$ mice contained elevated levels of unesterified cholesterol found in the WT meibum (Figure 4F). However, there were no significant variations in the triacylglycerol populations (Figure 4D).

To test whether these compensatory changes in the meibum in response to the absence of AWAT2 are associated with changes in fatty acid composition, we compared their profile and relative abundance. LC-MS analysis indicated a lack of significant discrepancies between WT and *Awat2*$^{-/-}$ mice except long monounsaturated chain fatty acids species (C26:1-C36:1) that were ~10× more abundant in the meibum of knockout animals (Figure S5A,B). Because of the inherent instability of cholesteryl esters during ionization they cannot be directly observed in MS spectra in our experimental setting. Thus, to determine the fatty acid profile of cholesteryl esters they were separated from other types of lipids by HPLC prior to hydrolysis. The composition of fatty acids liberated from cholesteryl esters collected from WT and *Awat2*$^{-/-}$ mice did not reveal major divergences (Figure S5C). The exceptions were fatty acids with acyl chains longer than 22 carbons, the relative abundance of which was much lower in cholesteryl esters isolated from *Awat2*$^{-/-}$ mice. Therefore, it is likely that the unsaturated acyl chains of wax diesters were the main contributors to the increase in the amount of total unsaturated fatty acids in the meibum of *Awat2*$^{-/-}$ mice.

The comparative analysis of meibum lipids clearly shows the importance of AWAT2 in the production of wax esters in the MGs. Moreover, the profound compensatory response to the absence of AWAT2 activity indicated the existence of a metabolic shunt in the MGs that channels the excess of fatty acids and long-chain alcohols into the production of alternative classes of lipids, predominantly cholesterol esters and wax diesters.

3.4 | Progression of the pathophysiological consequences of AWAT2-deficiency

The suboptimal formation of the tear film lipid layer seen in AWAT2-deficient mice had consequential long-term effects on the health of the ocular surface. Starting at the age of 3 months, 4 out of 5 *Awat2*$^{-/-}$ mice showed progressive deterioration of corneal integrity. Fluorescein slit-lamp examinations revealed punctuated isolated areas of amplified staining that enlarged over time and by the age of 6 months covered large portions of the cornea (Figure 5A). The corneal surface abnormalities appeared as opaque spots that eventually affected most of the exposed cornea, limiting its transparency (Figure 5B). These pathological changes were accompanied by prominent staining of conjunctival with fluorescein that can be related to progressive blepharitis and deterioration of the conjunctiva that lines the inside of the eyelids (Figure 5A). OCT examination of corneal morphology

clearly indicated a dramatic increase in the thickness of the cornea that was associated with the progressive disorganization of the laminar structure of its tissue (Figure 5C,D). The first differences upon the histological examination of corneal sections between *Awat2*$^{-/-}$ and WT mice can be seen as early as 14 weeks of age (Figure 5E). *Awat2*$^{-/-}$ mice showed a deterioration of the corneal surface, irregular epithelium cells, some granular deposits in the stroma layer. As the disease progressed, corneal integrity declined to lead to corneal erosions, large buildups of epithelium cells that protrude into the stroma layer, empty space between keratocytes and corneal collagen fibers, and large gaps compromising the stromal integrity (Figure 5E). Additionally, inflammatory leukocytes infiltration of the cornea was accompanied by the formation of lymphatic vessels within the cornea as evidence by staining with CD45 and LYVE-1 antibody (Figure 5E). In this severe stage, *Awat2*$^{-/-}$ mice also developed neovascularization of the cornea clearly seen upon slit-lamp and OCT examination (Figure 6A). In addition to considerable corneal pathology, *Awat2*$^{-/-}$ mice revealed symptoms of blepharitis macroscopically manifested by swollen and inflamed eyelids (Figure 6B). An anterior and posterior synechia was also observed in this stage of the disease (Figure 6C,D). The iris became split, leaving the posterior pigmented epithelium on the surface of the lens. Unexpectedly, posterior synechia can also be found in the early stage of the disease (Figure 6C).

Inflammation of the ocular surface can be considered a secondary effect of DED, but it had a detrimental effect on the progression of the pathophysiological changes in the eyes. The occurrence and severity of the inflammation were variable and most likely depended on environmental conditions such as housing, number of mice per cage, and frequency of eye scratching by individual mice. In our experimental conditions, severe inflammation of the ocular surface was evident in 4 out of 10 mice 9 months of age or older. However, isolated cases of inflammatory response also occurred in mice as young as 2 months. Immunofluorescence examination showed that it affected the tarsal plates and the MGs within them (Figure 6E). Importantly, the infiltration of CD45-positive immune cells had a detrimental effect on the rate of MG degeneration, greatly accelerating this process as compared to mice in which the inflammatory response was not as evident (Figures 3F,G and 6E,F). Notably, the overall severity of the ocular condition was directly correlated with the presence of an inflammatory response. Although mechanistically distinct, pathophysiological consequences of AWAT2 deficiency manifested by the susceptibility to corneal damage and ocular surface inflammation were related to the phenotype described for other mouse models of evaporative dry eye disease, including *Elovl1* and *Elovl3* conditional knockout mice.[31,32]

3.5 | The effect of AWAT2-deficiency on the skin

MGs are a subtype of the exocrine sebaceous gland (SG) present in the skin. By analogy to MGs, SGs are the primary site of AWAT2 expression (Figure 7A). Therefore, one could anticipate that the absence of AWAT2 will have an adverse effect on the skin. Surprisingly, the severity of the skin phenotype was relatively mild. It was manifested by scaly and dry skin predominantly on the tail (Figure 7B) and ears (Figure 7C). Notably, these cutaneous abnormalities became apparent in mice at the age of six months and older. By the age of 12 months, mice suffered from occasional lesions in the ear skin. *Awat2*$^{-/-}$ mice also displayed

partial fur loss that mainly affected the dorsal side of the neck (Figure 7D). Their hair was easily removable when pulled without force which was not the case in WT mice (Figure 7E). Histological sections showed patches of the thickened epidermis (Figure 7B,C) accompanied by the dilatation of hair follicles (Figure 7B). In comparison to WT mice, the skin sections of *Awat2*$^{-/-}$ mice revealed much smaller sebum-filled SGs even though the basaloid and germinative layer that gives rise to mature sebocytes was present indicating atrophic sebocytes (Figure 7F). A reduced number of SGs was also noticeable in *Awat2*$^{-/-}$ mice confirming SG atrophy.

4 | DISCUSSION

Neutral lipids are a highly diverse class of natural compounds formed by the esterification of a variety of alcohols (steroids, mono- and diacylglycerols, retinol, or long-chain alcohols) with fatty acids. In addition to their traditionally assigned lipid storage function, neutral lipids acquire a functional role in selected tissues, often as permeability barriers in the skin and the corneas of animals as well as the cuticles of plants. Multiple genes encoding acyltransferases are involved in the biosynthesis of neutral lipids and reveal overlapping substrate specificity.[33] For example, the existence of seemingly redundant enzymatic activity in the DGAT2 protein family does not allow for decisive predictions of the physiological functions of individual enzymes without considering tissue-specific expression, accessibility to substrates, or the regulation of the enzymatic activities in response to different stimuli. Thus, the ultimate confirmation of the role of individual enzymes in the metabolism of neutral lipids can be obtained only by investigating the phenotypic consequences of the inactivation of individual genes. AWAT2, one of the seven members of the DGAT2 protein family, has been proposed to catalyze the formation of wax esters, but its broad substrate specificity does not exclude the possibility that this enzyme is involved in the synthesis of other neutral lipids.[19–22] Hence, to obtain direct evidence of the role of the *Awat2* gene, we examined the phenotype of genetically modified mice lacking the functional enzyme.

As anticipated from the tissue expression patterns of AWAT2, restricted to the exocrine SGs and MGs,[20] the disruption of the *Awat2* gene affected the protective lipid layer of the skin and ocular surface. Notably, the pathophysiological consequences of AWAT2 deficiency were more profound in the eye as compared to the skin tissues. This difference is most likely related to the fact that wax esters represent only about 5% of total lipids in mouse sebum, whereas the fraction of wax esters in meibum is around 40%.[34] Interestingly, although the meibum composition is similar in mice and humans, the sebaceous lipids are enriched in wax esters to about 30% in human skin samples.[9,35–37] Thus, the mild skin phenotype observed in mice may be dramatically enhanced in humans. Nevertheless, the most direct characteristics of *Awat2*$^{-/-}$ mice is that they revealed early onset symptoms of evaporative DED that were accompanied by progressive corneal damage, degeneration of the MGs, and subsequent inflammatory response. The precipitating cause of the pathologies was directly related to the suboptimal lipid composition of the meibum that was deprived of the wax ester fraction. This direct observation clearly indicates that despite the high substrate promiscuity observed in vitro, AWAT2 is a non-redundant enzyme responsible for the biosynthesis of wax esters in the MGs and its physiological role cannot be substituted by the enzymatic activity of related AWAT1. Moreover, the absence of AWAT2 did not eliminate wax diesters

from the mouse meibum (Figure 4), confirming the previously reported lack of catalytic activity toward (*O*-Acyl)-ω-hydroxy alcohols.[19]

Interestingly, the inability to produce wax esters resulted not only in a meibum depleted of this class of lipids, but also caused a profound alteration in the lipid profile and in turn the biophysical properties of MG secretion. In *Awat2*$^{-/-}$ mice, the wax ester fraction was replaced by an increased amount of cholesteryl esters by a compensatory mechanism. Although the total fatty acid distribution remained largely unchanged, an 8-times higher amount of cholesteryl esters considerably increases the viscosity of the meibum as melting points for this class of lipids is much higher than for the corresponding wax esters. For example, the reported melting temperature for cholesteryl ester carrying a C18:0 fatty acid moiety is 81.5°C, whereas, for the prototypical wax ester, oleyl stearate is only 23.8°C.[38,39] Thus, the abnormally high ratios of cholesteryl esters to other lipids can affect the stability of the tear film, limiting its protective effect, but more critically causing an over-accumulation of lipids in the central duct and its obstruction as evident in the *Awat2*$^{-/-}$ mice (Figure 2). Importantly, increased meibum viscosity is commonly observed in the pathogenesis of MG dysfunction in humans.[40–43] It can be caused by an age-related quantitative change in lipid profile that leads to the thickening of the meibum and initiation or further worsening of MG obstruction.[44] Prolonged stasis of meibum inside the MG has long-lasting consequences for the function and structural integrity of the acini.[6,45,46] Continuous secretion of highly viscous meibum by the acini leads to a buildup of pressure inside the central duct of the MG and its dilation. Atrophy of the acini is a long-term consequence of lipid stenosis and an increase in intraglandular pressure, clinically observed as MG dropout. In its final stage, the duct's walls become cornified and the meibocytes are replaced with stratified squamous epithelium. Notably, the above natural history of MG dysfunction is closely recapitulated in *Awat2*$^{-/-}$ mice. Although obstructive DED can be induced in animals, for example by the treatment of rabbit's eyelids with epinephrine or the inactivation of the *Hr* gene (rhino mouse), ocular pathologies in these models are caused solely by the augmented keratinization of the MG orifice or its ducts.[47,48] In contrast, the symptoms of obstructive DED seen in *Awat2*$^{-/-}$ mice are exclusively related to the suboptimal lipid composition of meibum. Surprisingly, the obstructive form of evaporative DED was not reported for conditional knockout mice lacking fatty acid elongase genes, *Elovl1* or *Elovl3,* even though both of these mouse lines exhibit symptoms of DED due to the shortening of the chain length of meibum lipids.[31,32] However, the obstruction of MG orifices with white, semiliquid discharge was one of the phenotypic features of mice deficient in CYP4f39, a P450 cytochrome that exhibits ω-hydroxylase activity toward long-chain fatty acids.[49] In this newly established model of evaporative DED, the meibum was depleted of ω-hydroxy fatty acids and their subsequent metabolites such as (*O*-Acyl)-ω-hydroxy fatty acids, wax diesters, and cholesteryl (*O*-Acyl)-ω-hydroxy fatty acids.

Although MG dysfunction is the most common cause of DED, there are no effective therapies targeting the underlying cause of this eye condition.[6,50] Therefore, broadening our knowledge about the biogenesis and function of tear film lipids is essential for proposing and testing new therapeutic strategies. In this context, the development of animal models that resemble obstructive DED such as *Awat2*$^{-/-}$ or *Cyp4f39*$^{-/-}$ mice is a significant step

forward toward a better understanding of the principles of lipid synthesis in the MGs as well as bringing hope for designing new therapeutic strategies to prevent or combat DED.

Supplementary Material

Refer to Web version on PubMed Central for supplementary material.

ACKNOWLEDGMENTS

We thank Catherine Doller, Anthony Gardella, and Maryanne Pendergast from the Visual Science Core Facility at CWRU for their expert help with histology, microscopy, and imaging. Also, we would like to acknowledge Wiktor Golczak for his contribution to the editing of this manuscript. This work was supported by the EY023948 grant from the National Eye Institute of the National Institutes of Health (MG) as well as the Visual Sciences Research Center Core Facilities that were funded by NIH P30 core grant EY011373.

Funding information

HHS | NIH | National Eye Institute (NEI), Grant/Award Number: EY023948 and EY011373

Abbreviations

AWAT2	acyl-CoA wax alcohol acyltransferase 2
DED	dry eye disease
DGAT2	acyl-CoA diacylglycerol acyltransferase 2
H&E	Hematoxylin and Eosin staining
LC-MS	liquid chromatography-mass spectrometry
MFAT	multifunctional *O*-acyltransferase
MG	meibomian gland
MS	mass spectrometry
PRT	phenol red thread
SDOCT	spectral-domain optical coherence tomography
SG	sebaceous gland
TFBUT	tear film break-up time

REFERENCES

1. Dilly PN. Structure and function of the tear film. Adv Exp Med Biol. 1994;350:239–247. [PubMed: 8030483]
2. Knop E, Knop N, Schirra F. Meibomian glands. Part II: physiology, characteristics, distribution and function of meibomian oil. Ophthalmologe. 2009;106:884–892. [PubMed: 19856011]
3. Bron AJ, Tiffany JM, Gouveia SM, Yokoi N, Voon LW. Functional aspects of the tear film lipid layer. Exp Eye Res. 2004;78:347–360. [PubMed: 15106912]
4. Nelson JD, Shimazaki J, Benitez-del-Castillo JM, et al. The international workshop on meibomian gland dysfunction: report of the definition and classification subcommittee. Invest Ophthalmol Vis Sci. 2011;52:1930–1937. [PubMed: 21450914]

5. Knop N, Knop E. Meibomian glands. Part I: anatomy, embryology and histology of the Meibomian glands. Ophthalmologe. 2009;106:872–883. [PubMed: 19856010]
6. Knop E, Knop N, Millar T, Obata H, Sullivan DA. The international workshop on meibomian gland dysfunction: report of the subcommittee on anatomy, physiology, and pathophysiology of the meibomian gland. Invest Ophthalmol Vis Sci. 2011;52:1938–1978. [PubMed: 21450915]
7. Butovich IA, McMahon A, Wojtowicz JC, Lin F, Mancini R, Itani K. Dissecting lipid metabolism in meibomian glands of humans and mice: an integrative study reveals a network of metabolic reactions not duplicated in other tissues. Biochim Biophys Acta. 2016;1861:538–553. [PubMed: 27032494]
8. Butovich IA. Tear film lipids. Exp Eye Res. 2013;117:4–27. [PubMed: 23769846]
9. Butovich IA, Lu H, McMahon A, Eule JC. Toward an animal model of the human tear film: biochemical comparison of the mouse, canine, rabbit, and human meibomian lipidomes. Invest Ophthalmol Vis Sci. 2012;53:6881–6896. [PubMed: 22918629]
10. Schaumberg DA, Sullivan DA, Buring JE, Dana MR. Prevalence of dry eye syndrome among US women. Am J Ophthalmol. 2003;136:318–326. [PubMed: 12888056]
11. Schaumberg DA, Dana R, Buring JE, Sullivan DA. Prevalence of dry eye disease among US men: estimates from the Physicians' Health Studies. Arch Ophthalmol. 2009;127:763–768. [PubMed: 19506195]
12. Baudouin C The pathology of dry eye. Surv Ophthalmol. 2001;45(Suppl 2):S211–S220. [PubMed: 11587145]
13. Whitcher JP, Srinivasan M, Upadhyay MP. Corneal blindness: a global perspective. Bull World Health Organ. 2001;79:214–221. [PubMed: 11285665]
14. Lemp MA, Crews LA, Bron AJ, Foulks GN, Sullivan BD. Distribution of aqueous-deficient and evaporative dry eye in a clinic-based patient cohort: a retrospective study. Cornea. 2012;31:472–478. [PubMed: 22378109]
15. Kaercher T, Bron AJ. Classification and diagnosis of dry eye. Dev Ophthalmol. 2008;41:36–53. [PubMed: 18453760]
16. Schirra F, Richards SM, Sullivan DA. Androgen influence on cholesterogenic enzyme mRNA levels in the mouse meibomian gland. Curr Eye Res. 2007;32:393–398. [PubMed: 17514523]
17. Schirra F, Suzuki T, Richards SM, et al. Androgen control of gene expression in the mouse meibomian gland. Invest Ophthalmol Vis Sci. 2005;46:3666–3675. [PubMed: 16186348]
18. Butovich IA. Lipidomics of human Meibomian gland secretions: chemistry, biophysics, and physiological role of Meibomian lipids. Prog Lipid Res. 2011;50:278–301. [PubMed: 21458488]
19. Yen CL, Brown CHT, Monetti M, Farese RV Jr. A human skin multifunctional O-acyltransferase that catalyzes the synthesis of acylglycerols, waxes, and retinyl esters. J Lipid Res. 2005;46:2388–2397. [PubMed: 16106050]
20. Turkish AR, Henneberry AL, Cromley D, et al. Identification of two novel human acyl-CoA wax alcohol acyltransferases: members of the diacylglycerol acyltransferase 2 (DGAT2) gene superfamily. J Biol Chem. 2005;280:14755–14764. [PubMed: 15671038]
21. Arne JM, Widjaja-Adhi MA, Hughes T, et al. Allosteric modulation of the substrate specificity of acyl-CoA wax alcohol acyltransferase 2. J Lipid Res. 2017;58:719–730. [PubMed: 28096191]
22. Kaylor JJ, Cook JD, Makshanoff J, Bischoff N, Yong J, Travis GH. Identification of the 11-cis-specific retinyl-ester synthase in retinal Muller cells as multifunctional O-acyltransferase (MFAT). Proc Natl Acad Sci U S A. 2014;111:7302–7307. [PubMed: 24799687]
23. Vincent SD, Robertson EJ. Highly efficient transgene-independent recombination directed by a maternally derived SOX2CRE transgene. Genesis. 2003;37:54–56. [PubMed: 14595840]
24. Hayashi S, Tenzen T, McMahon AP. Maternal inheritance of Cre activity in a Sox2Cre deleter strain. Genesis. 2003;37:51–53. [PubMed: 14595839]
25. Amengual J, Zhang N, Kemerer M, Maeda T, Palczewski K, Von Lintig J. STRA6 is critical for cellular vitamin A uptake and homeostasis. Hum Mol Genet. 2014;23:5402–5417. [PubMed: 24852372]
26. Sakamoto R, Bennett ES, Henry VA, et al. The phenol red thread tear test: a cross-cultural study. Invest Ophthalmol Vis Sci. 1993;34:3510–3514. [PubMed: 8258507]

27. Holmes RS. Comparative genomics and proteomics of vertebrate diacylglycerol acyltransferase (DGAT), acyl CoA wax alcohol acyltransferase (AWAT) and monoacylglycerol acyltransferase (MGAT). Comp Biochem Physiol Part D Genomics Proteomics. 2010;5:45–54. [PubMed: 20374941]
28. Hayashi S, Lewis P, Pevny L, McMahon AP. Efficient gene modulation in mouse epiblast using a Sox2Cre transgenic mouse strain. Mech Dev. 2002;119(Suppl 1):S97–S101. [PubMed: 14516668]
29. Butovich IA. Lipidomic analysis of human meibum using HPLC-MSn. Methods Mol Biol. 2009;579:221–246. [PubMed: 19763478]
30. Chen J, Panthi S. Lipidomic analysis of meibomian gland secretions from the tree shrew: Identification of candidate tear lipids critical for reducing evaporation. Chem Phys Lipids. 2019;220:36–48. [PubMed: 30660743]
31. Sassa T, Tadaki M, Kiyonari H, Kihara A. Very long-chain tear film lipids produced by fatty acid elongase ELOVL1 prevent dry eye disease in mice. FASEB J. 2018;32:2966–2978. [PubMed: 29401594]
32. Butovich IA, Wilkerson A, Bhat N, McMahon A, Yuksel S. On the pivotal role of Elovl3/ELOVL3 in meibogenesis and ocular physiology of mice. FASEB J. 2019;33:10034–10048. [PubMed: 31208226]
33. Turkish AR, Sturley SL. The genetics of neutral lipid biosynthesis: an evolutionary perspective. Am J Physiol Endocrinol Metab. 2009;297:E19–E27. [PubMed: 19116372]
34. Butovich IA. Meibomian glands, meibum, and meibogenesis. Exp Eye Res. 2017;163:2–16. [PubMed: 28669846]
35. Camera E, Ludovici M, Galante M, Sinagra JL, Picardo M. Comprehensive analysis of the major lipid classes in sebum by rapid resolution high-performance liquid chromatography and electrospray mass spectrometry. J Lipid Res. 2010;51: 3377–3388. [PubMed: 20719760]
36. Smith KR, Thiboutot DM. Thematic review series: skin lipids. Sebaceous gland lipids: friend or foe? J Lipid Res. 2008;49:271–281. [PubMed: 17975220]
37. Pappas A Epidermal surface lipids. Dermatoendocrinol. 2009;1:72–76. [PubMed: 20224687]
38. Iyengar BT, Schlenk H. Melting points of synthetic wax esters. Lipids. 1969;4:28–30. [PubMed: 5766845]
39. Mahadevan V, Lundberg WO. Preparation of cholesterol esters of long-chain fatty acids and characterization of cholesteryl arachidonate. J Lipid Res. 1962;3:106.
40. Foulks GN, Bron AJ. Meibomian gland dysfunction: a clinical scheme for description, diagnosis, classification, and grading. Ocul Surf. 2003;1:107–126. [PubMed: 17075643]
41. Shimazaki J, Sakata M, Tsubota K. Ocular surface changes and discomfort in patients with meibomian gland dysfunction. Arch Ophthalmol. 1995;113:1266–1270. [PubMed: 7575257]
42. Ngo W, Srinivasan S, Schulze M, Jones L. Repeatability of grading meibomian gland dropout using two infrared systems. Optom Vis Sci. 2014;91:658–667. [PubMed: 24830370]
43. Feng Y, Gao Z, Feng K, Qu H, Hong J. Meibomian gland dropout in patients with dry eye disease in China. Curr Eye Res. 2014;39:965–972. [PubMed: 25051400]
44. Sullivan BD, Evans JE, Dana MR, Sullivan DA. Influence of aging on the polar and neutral lipid profiles in human meibomian gland secretions. Arch Ophthalmol. 2006;124:1286–1292. [PubMed: 16966624]
45. Knop E, Knop N. Meibomian glands : part IV. Functional interactions in the pathogenesis of meibomian gland dysfunction (MGD). Ophthalmologe. 2009;106:980–987. [PubMed: 19941141]
46. Blackie CA, Korb DR, Knop E, Bedi R, Knop N, Holland EJ. Nonobvious obstructive meibomian gland dysfunction. Cornea. 2010;29:1333–1345. [PubMed: 20847669]
47. Jester JV, Rife L, Nii D, Luttrull JK, Wilson L, Smith RE. In vivo biomicroscopy and photography of meibomian glands in a rabbit model of meibomian gland dysfunction. Invest Ophthalmol Vis Sci. 1982;22:660–667. [PubMed: 7076409]
48. Jester JV, Rajagopalan S, Rodrigues M. Meibomian gland changes in the rhino (hrrhhrrh) mouse. Invest Ophthalmol Vis Sci. 1988;29:1190–1194. [PubMed: 2458328]
49. Miyamoto M, Sassa T, Sawai M, Kihara A. Lipid polarity gradient formed by omega-hydroxy lipids in tear film prevents dry eye disease. Elife. 2020;9.

50. Bron AJ, Tiffany JM. The contribution of meibomian disease to dry eye. Ocul Surf. 2004;2:149–165. [PubMed: 17216085]

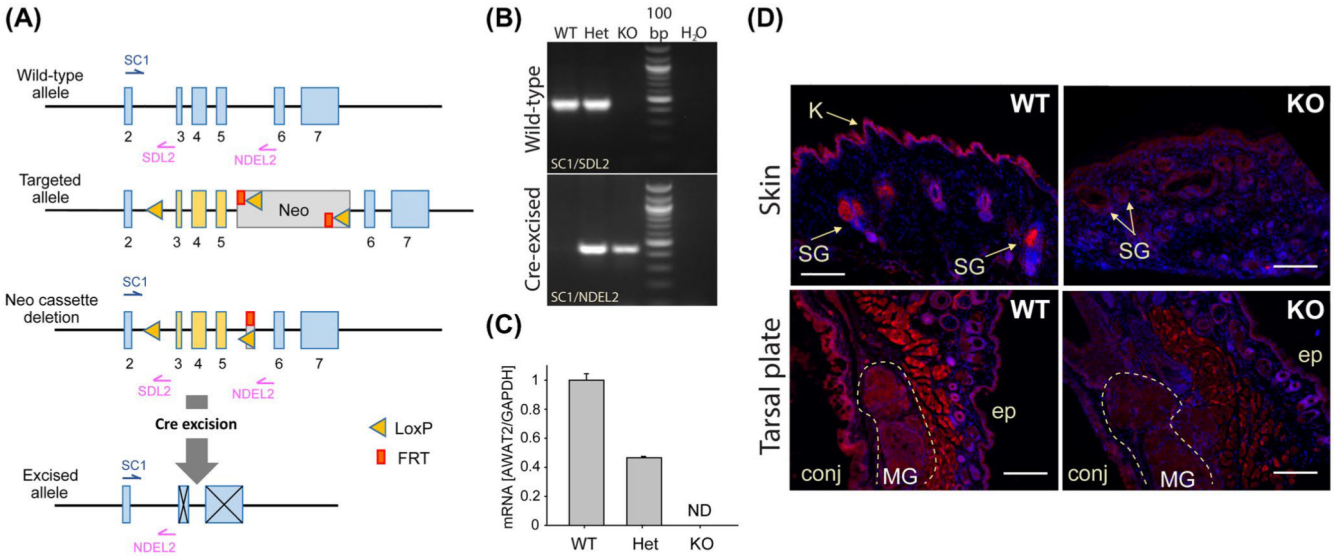

FIGURE 1. Generation and validation of the Awat2$^{-/-}$ knockout mice.

A, LoxP/FRT-flanked Neo cassette was inserted 351 bp downstream of exon 5 and a single LoxP site was inserted 371 bp upstream of exon 3. The target region contains exons 3–5. A null (global) excised allele was generated by crossing the homozygous LoxP mice with Sox2-Cre mice. B, Gel image of genomic PCR using SC1, SDL2, and NDEL2 primers. C, The absence of *Awat2* transcript in genetically modified mice used in the study was verified by RT-qPCR and (D) immunofluorescence of mouse skin and tarsal plate, AWAT2 (red) and nuclei (DAPI, blue). Scale bar corresponds to 1 mm; SG—sebaceous gland; K—keratinocytes; MG—meibomian glands, bp—base pair; conj—conjunctiva, and Het—*Awat2*$^{+/-}$

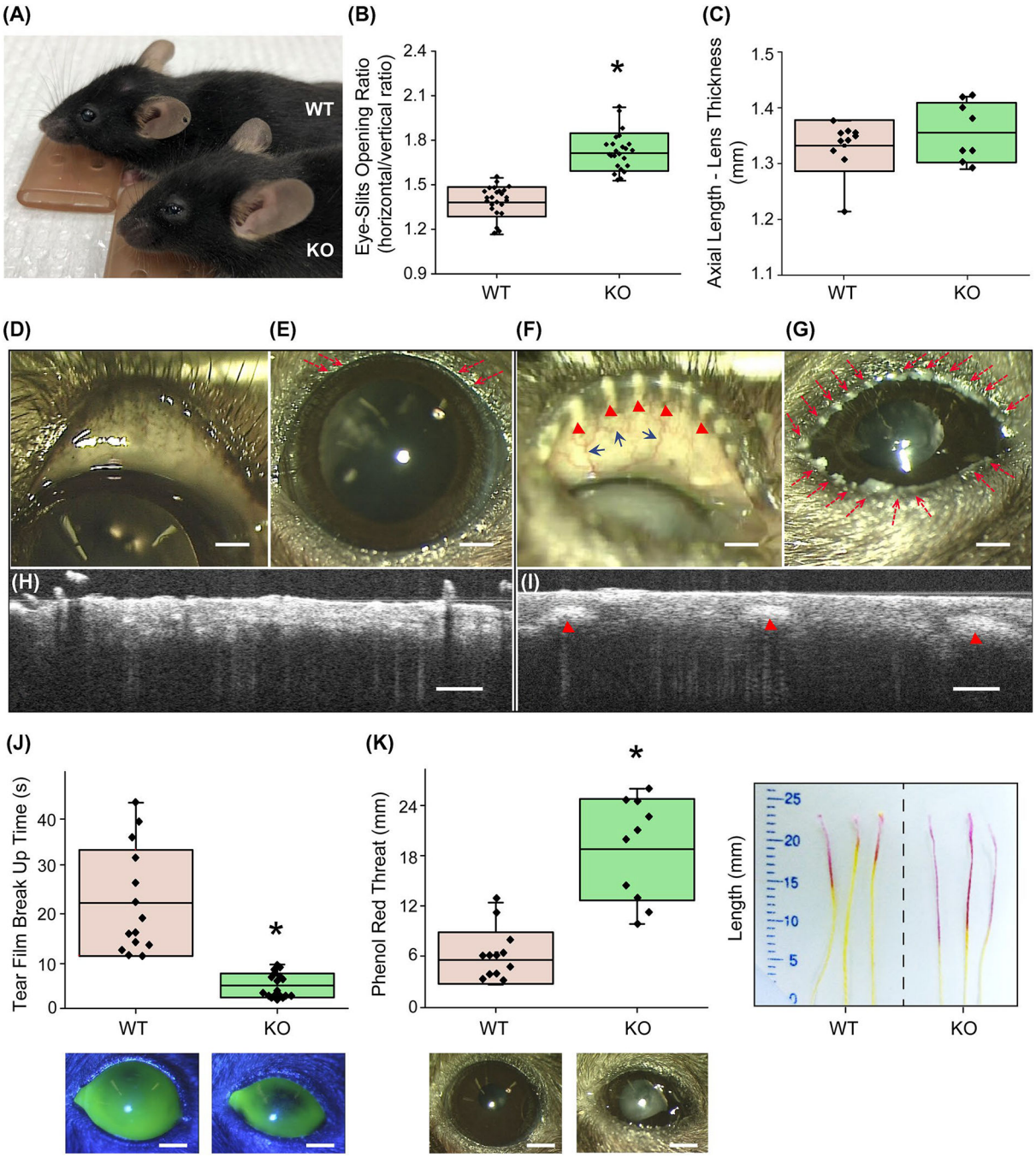

FIGURE 2. Awat2$^{-/-}$ mice exhibit an evaporative dry eye phenotype related to obstructive meibomian gland (MG) dysfunction.

A, Photographs of gross phenotypic differences of *Awat2*$^{-/-}$ mice with a slit-like eye distinctive from the wide-open eye of WT mice. B, Measurement of the eye-slits opening ratio of WT (n = 24; 10 females, 14 males; 12 OS, 12 OD) and *Awat2*$^{-/-}$ (n = 24; 12 females, 12 males; 12 OS, 12 OD) mice. C, Axial length measurement of the eyeball without the lens of WT (n = 10; 6 females, 4 males; 5 OS, 5 OD) and *Awat2*$^{-/-}$ (n = 8; 6 females, 2 males; 4 OS, 4 OD) mice. Representative images of the eye, tarsal plate, and MG orifice (red dashed line arrows) of WT (D, E) and *Awat2*$^{-/-}$ mice (F, G). *Awat2*$^{-/-}$ mice reveal

obstructive MG orifice caused by the accumulation of white deposits within the duct of the MG (red arrowheads) and occurrence of telangiectasia (blue arrows). MG plugging (red arrowheads) are clearly seen in the OCT image of *Awat2*$^{-/-}$ mice (I), but was not observed in WT mice (H). J, Tear film break-up time was measured from 4-month old WT (n = 14; 4 females, 10 males; 7 OS, 7 OD) and *Awat2*$^{-/-}$ (n = 18; 10 females, 8 males; 10 OS, 8 OD) mice. The insets represent photographs of eye after the break-up of fluorescein stained tear film. K, Phenol red thread test was used to assess tearing in tested mice. The experiments were performed on 4-month old WT (n = 12; 6 females, 6 males; 6 OS, 6 OD) and *Awat2*$^{-/-}$ (n = 10; 6 females, 4 males; 5 OS, 5 OD) mice. Insets show pictures of mouse eyes before the test (below) and the representative PRT image (right) used for ImageJ analysis. OS (oculus sinister) means the left eye and OD (oculus dextrus) means the right eye. Scale bars represent 0.5 mm. (*) indicates statistical significance ($P < .001$) by One-Way ANOVA followed by the Scheffe test

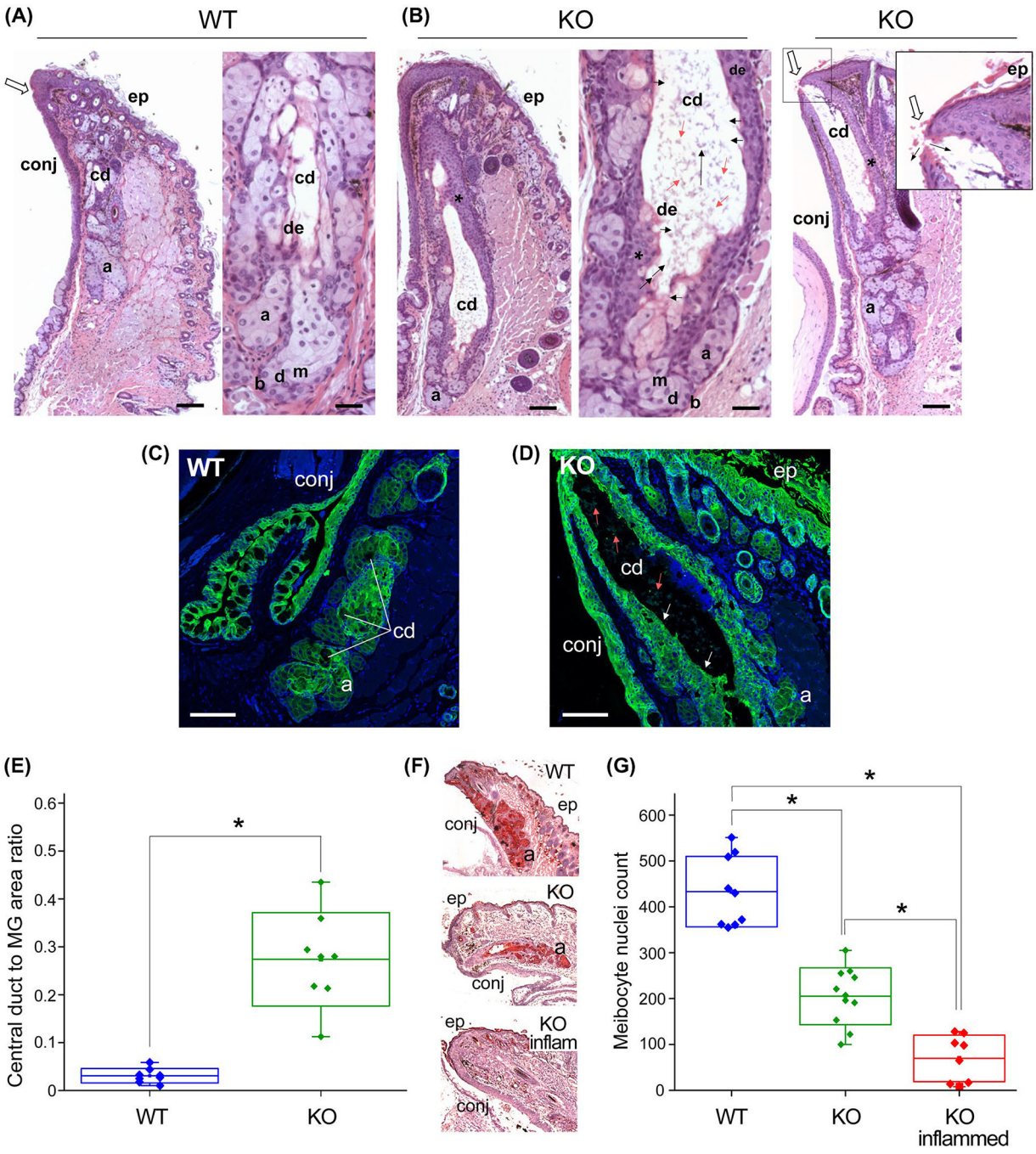

FIGURE 3. Morphological changes within MG associated with AWAT2-deficiency.

Representative histology sections of the tarsal plate of WT and *Awat2*$^{-/-}$ mice (2-month old) stained with H&E. A, Normal histological appearance of the acini (a), orifice (open arrow), connecting ductal (de), central duct (cd) of MG of WT mice; b—base cells, d—differentiating meibocytes, ep—epidermis; m—mature meibocyte; ep—epithelium; conj—conjunctiva; open arrow points toward the orifice. B, As compared to the WT control, histological analysis of the tarsal plates isolated form *Awat2*$^{-/-}$ mice revealed dilatation of the central duct, ductal epithelium cornification (*), accumulation of keratin debris (red

arrows) inside the duct lumen from the hyperkeratinized ductal wall, and atrophy of the acini (a). These pathological changes are most likely caused by the secretion of suboptimal meibum that leads to blockage of the ducts, increased pressure inside the glands, and a gradual dilatation of the central duct. C, D, Representative keratin 6a immunofluorescence of tarsal plate isolated from WT and *Awat2*$^{-/-}$ mice (keratin 6a shown in green, nuclei stained in blue by DAPI). Robust stain of the cells lining the dilated central duct of keratin 6a (marked with white arrows) in *Awat2*$^{-/-}$ mice confirms the thickening of the epithelium layer anticipated based on the morphological images shown in panel B. Also, cellular debris imaged by H&E staining show immunoreactivity toward keratin 6a (red arrows), indicating the accumulation of keratin debris inside the duct lumen. E, Quantification of the central duck dilation. The data represent ratios between the cross-sectional areas of the central duct and the total area of MG calculated based on histology slides for WT (n = 8; 4 females, 4 males; 4 OS, 4 OD) and *Awat2*$^{-/-}$ (n = 8; 3 females, 5 males; 4 OS, 4 OD) mice. F, Representative Oil-Red-O lipid staining in WT and AWAT2-deficient mouse reveal degeneration of the meibum-producing acini. G, Quantification of the degeneration of the MGs represented as number of meibocytes found in the tarsal plate sections of WT (n = 9; 2 females, 7 males; 4 OS, 5 OD), non-inflammed *Awat2*$^{-/-}$ (n = 11; 3 females, 8 males; 5 OS, 6 OD), and inflamed *Awat2*$^{-/-}$ (n = 8; 7 females, 1 male; 2 OS, 6 OD) mice. For MG degeneration analysis, we incorporated data obtained for mice at the age between 4 and 9 months. In the boxplot-and-whiskers graphs shown in this figure, the boxes represent standard deviation values, the mean is marked by a vertical line inside the box, whereas the whiskers correspond to min and max values. Scale bars correspond to 0.1mm in panel A (left image), panel B (left and right image), panel C, and panel D; 0.05 mm in panels A (right image) and panel B (middle and the inset of right image). (*) indicates statistical significance ($P < .001$) by One-Way ANOVA followed by the Scheffe test

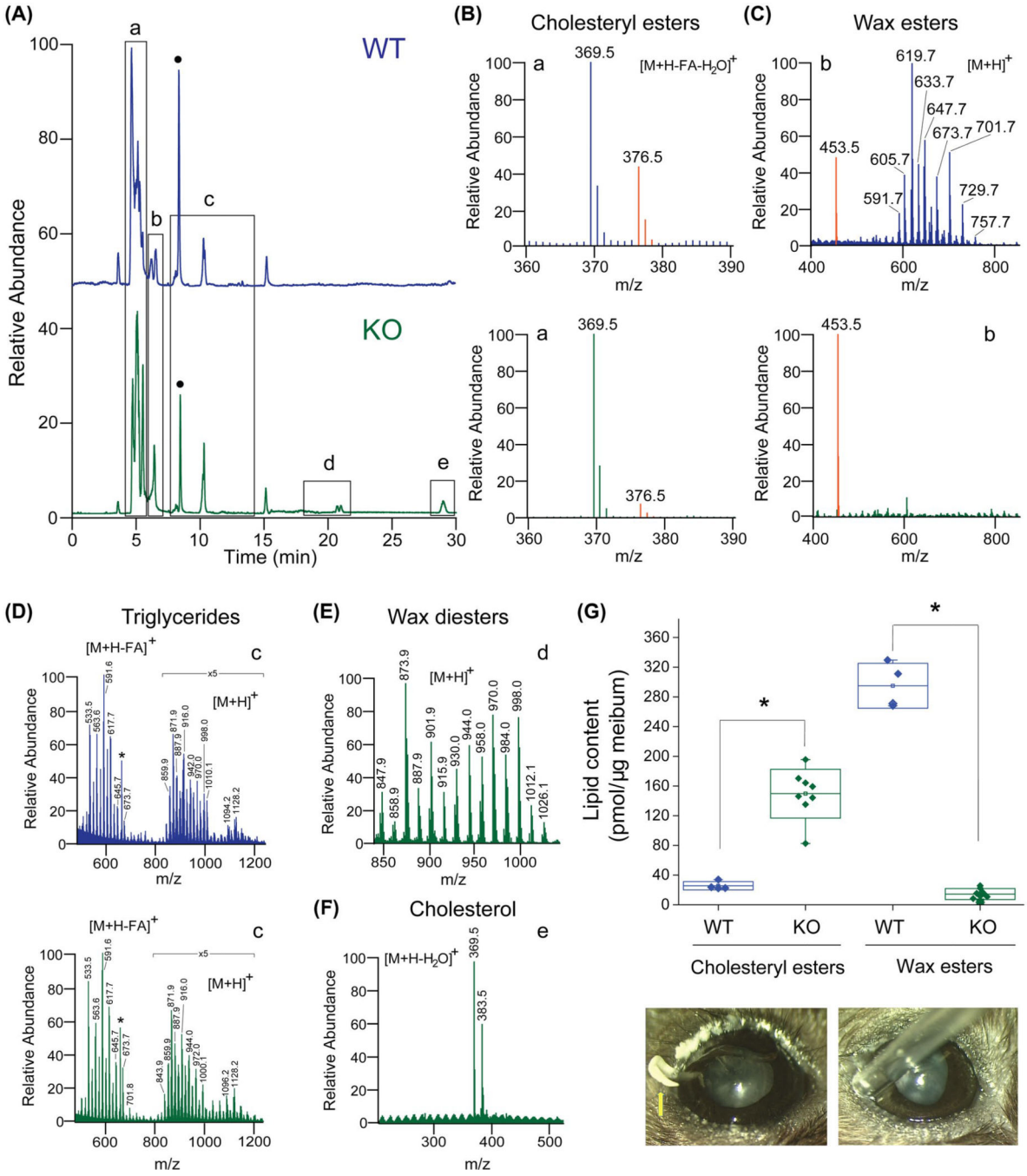

FIGURE 4. Detection and quantification of changes in lipid components of meibum in AWAT2-deficient mice.

Meibum was collected from 4-month old mice. Neutral lipids present in the hexanoic extracts from meibum samples were separated and analyzed by LC/MS. A, The elution profile of nonpolar lipids isolated from WT (blue trace) and *Awat2*$^{-/-}$ (green) mice. Five main classes of lipids were readily detectable in the analyzed samples: cholesteryl esters (a), wax esters (b), triglycerides (c), wax diesters (d), and unesterified cholesterol (e). (●) relates to m/z = 664.0 ion ($[M + H]^+$), a common plasticizer contaminant. B, Internal standard-based quantification of cholesteryl esters. MS spectra illustrates the relationship between the

$[M + H - FA - H_2O]^+$ ions corresponding to the internal standard (m/z = 376.5, cholesteryl-d7 palmitate) and naturally occurring cholesteryl esters (m/z = 369.5). The intensities of these ions served to calculate the amount of cholesteryl esters in the analyzed biological samples. C, Quantification of wax ester fraction of meibum. WT meibum samples contain the dominant fraction of wax esters that are readily detectable as a characteristic distribution of $[M + H]^+$ ions. They are greatly diminished in samples obtained from *Awat2*$^{-/-}$ mice. Ion at m/z = 453.5 corresponds to myristyl palmitate that served as an internal standard. D, Fraction of triglycerides identified in the meibum isolated from WT and *Awat2*$^{-/-}$ mice do not reveal significant differences (colored blue and green, respectively). E, MS spectrum of wax diesters found in the meibum from *Awat2*$^{-/-}$ mice. F, Unesterified cholesterol along with its oxidized forms (m/z = 369.5 and 383.5, respectively) was readily detectable in the examined samples. G, Boxplot-and-whiskers graph that summarizes the difference in lipid composition between WT (n = 4) and AWAT2-deficient (n = 8) mice. The (n) indicate the number of biological replicates. Each replicate was a pool of meibum collected from five mice (3 males and 2 females). The boxes represent mean and standard deviation values, whereas the whiskers correspond to min and max values. The photographs show the consistency of meibum gently squeezed and collected from obstructed MGs of AWAT2-deficient mice (yellow arrow). (*) indicates statistical significance ($P < .001$) by One-Way ANOVA followed by the Scheffe test

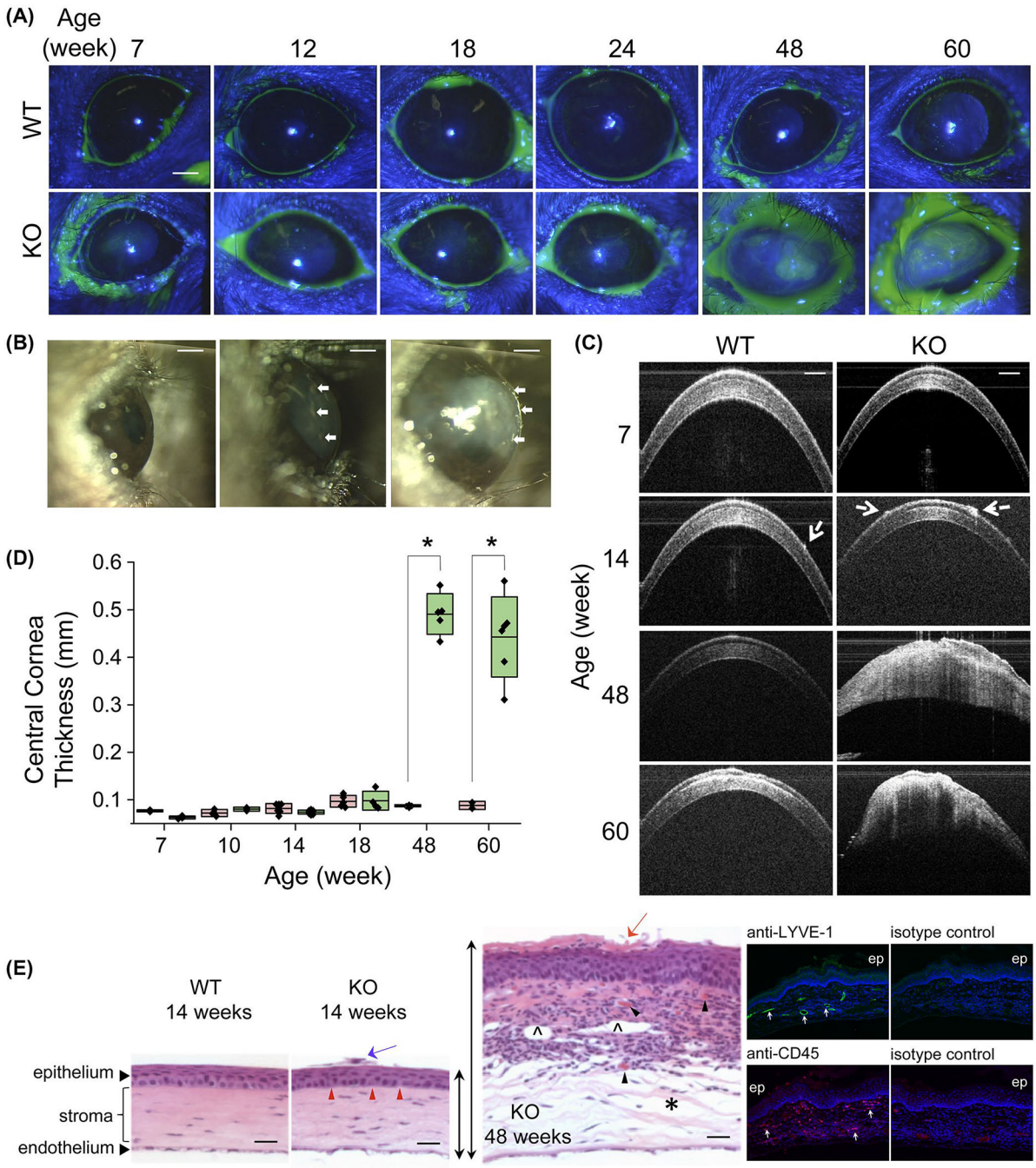

FIGURE 5. Corneal integrity deterioration of aged Awat2$^{-/-}$ mice.

A, Representative fluorescein-dye staining image of ocular surface *Awat2*$^{-/-}$ mice and age-matched WT control mice at different time-points. Punctuated areas of retained fluorescence dye represent compromised integrity of the corneal surface in *Awat2*$^{-/-}$ mice. B, Slit-lamp photograph shows irregular ocular surface (arrows) and deterioration of cornea integrity in *Awat2*$^{-/-}$ mice. Scale bar—0.5 mm. C, Representative SDOCT images of cornea of *Awat2*$^{-/-}$ mice and age- matched WT controls at different time-points indicate progressive thickening and degeneration of the cellular structure of this tissue. Although, no

abnormalities were observed in the cornea of young mice (7-week old), the layer structure was severely disorganized in the aged *Awat2*$^{-/-}$ mice (48- and 60-week old). Arrows represent occurrences of ocular surface abnormalities that progress in *Awat2*$^{-/-}$ mice (starting at the age of 14 weeks). Scale bar—0.25 mm. D, Central cornea thickness was quantified in *Awat2*$^{-/-}$ mice (n = 3–8) and age-matched WT controls (n = 3–6) at different time-points. The boxes represent mean and standard deviation values, whereas the whiskers correspond to min and max values. (*) indicates statistical significance ($P < .001$) by One-Way ANOVA followed by the Scheffe test. E, Paraffin sections of WT and *Awat2*$^{-/-}$ mice cornea were stained with H&E. Bright-field images of a cornea structure of 14-week-old WT (left panel), 14-week-old *Awat2*$^{-/-}$ (middle), and 48-week-old *Awat2*$^{-/-}$ mice (right). The presence of punctuated epithelial abnormalities (blue arrow) and irregular epithelium cells (red arrowheads) was clearly apparent in the early stages of the pathology. Later, the boundary between the epithelium and stroma was lost due to a large number of cells irregularly distributed in these layers. Additionally, corneal erosions (orange arrow), the appearance of empty spaces between keratocytes and corneal collagen fibers (*), lymphatic vessels (^), and blood capillaries (black arrowheads) were common features of affected cornea in 48-week-old *Awat2*$^{-/-}$ mice. Scale bars—0.1 mm. The presence of the lymphatics and infiltration of the cornea with hematopoietic cell was further confirmed by immunofluorescence staining with anti-LYVE-1 and anti-CD45 antibodies, respectively. Blue color represents the staining of nuclei with DAPI

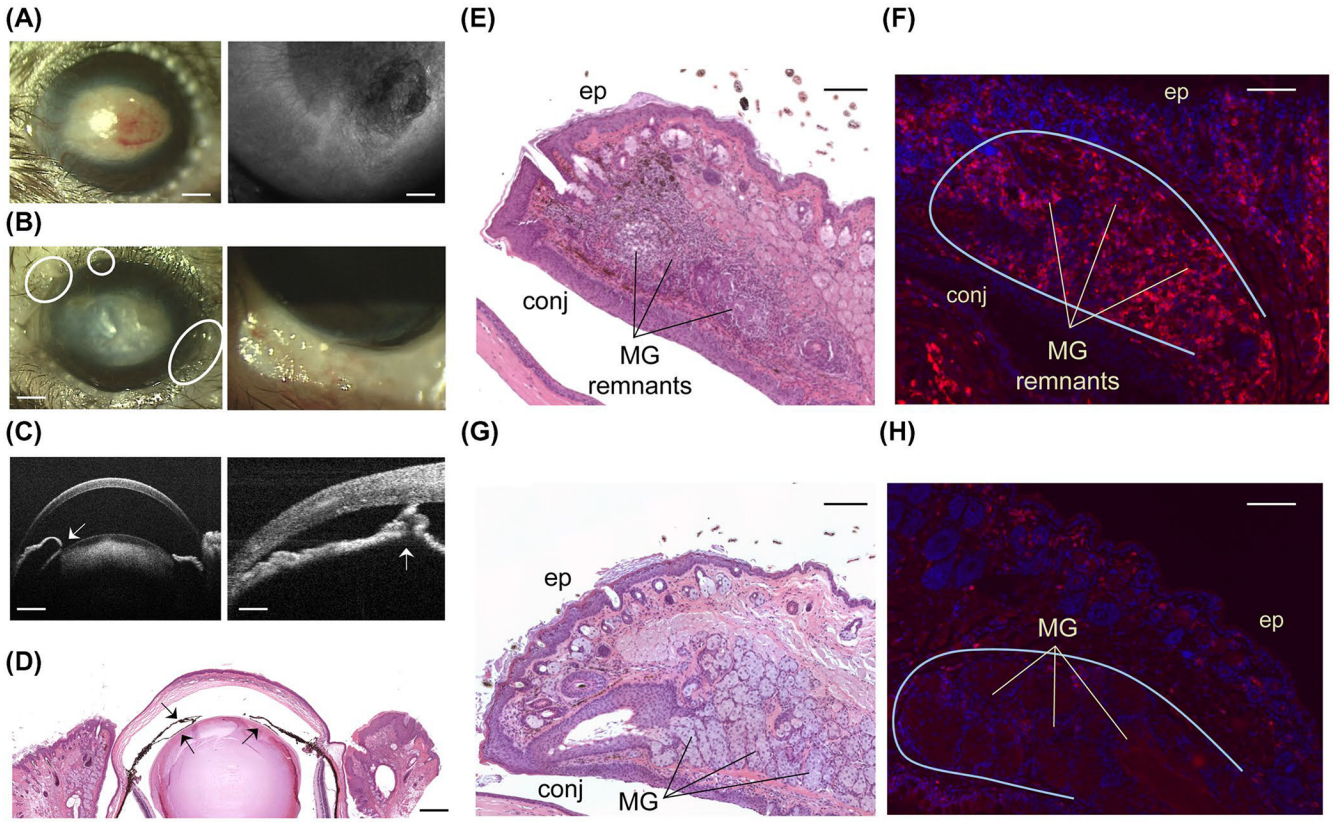

FIGURE 6. Severe progressive MG degeneration of Awat2$^{-/-}$ mice accompanied by an inflammatory response.

A, Photograph image of neovascularization in the cornea of 10-month old mice *Awat2*$^{-/-}$ mice using slit-lamp (left panel) and SDOCT (right). B, Photograph image of swollen, inflamed eyelid margins accompanied by MG dropout (circle). C, SDOCT image of a posterior synechia (left panel) and anterior synechia (right) observed in 3-month old and 10-month old AWAT2-deficient animals, respectively. Scale bars—0.5 mm (left) and 0.1 mm (right panel). D, Bright-field images of the anterior section of eyeball and tarsal plate of 14-month old *Awat2*$^{-/-}$ mice. Arrows indicate posterior synechia and split iris. Scale bars correspond to 0.25 mm. E-F, Bright-field and anti-CD45 immunofluorescence (in red, nuclei stained in blue by DAPI) images of inflamed MGs of 10-month old *Awat2*$^{-/-}$ mice and (G-H) non-inflamed MGs of 14-month old *Awat2*$^{-/-}$ mice. Scale bars in panels G-H—0.1 mm

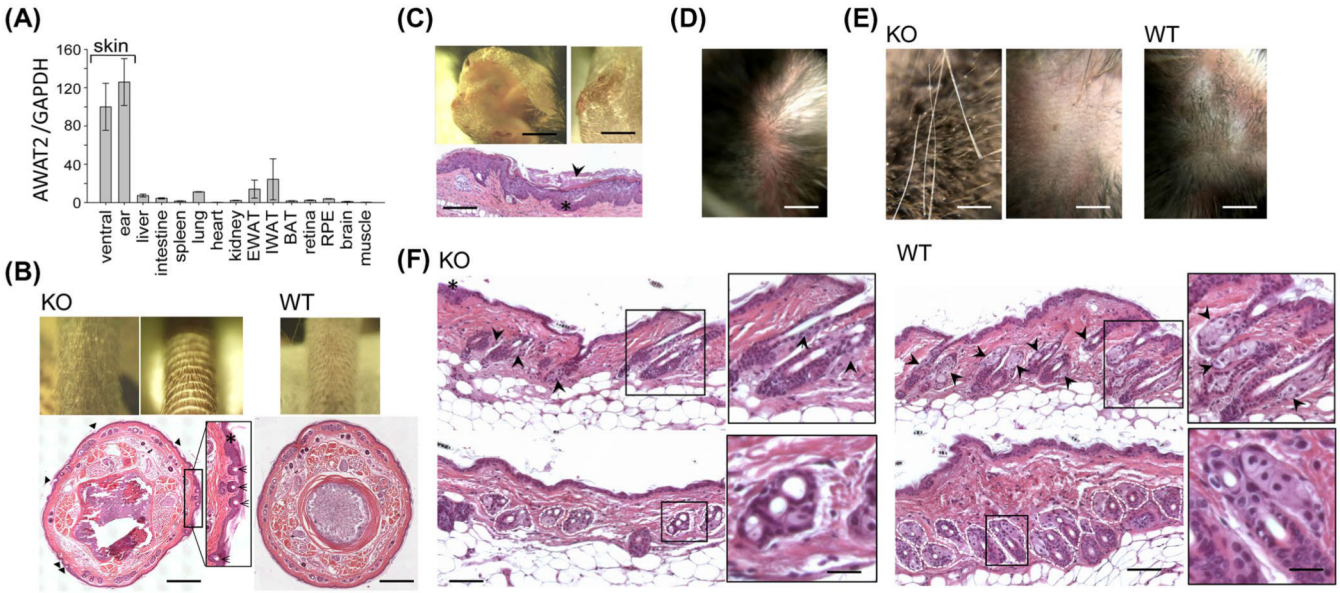

FIGURE 7. Skin phenotype related to SG degeneration in Awat2$^{-/-}$ mice.

A, Comparison of total *Awat2* mRNA levels in selected tissues; (EWAT) epididymal white adipose tissue, (IWAT) inguinal white adipose tissue, (BAT) brown adipose tissue, (RPE) retinal pigment epithelium. B, Picture of tail of *Awat2*$^{-/-}$ (upper left and middle panel) and WT (right panel). Paraffin cross-sections of the tail of 2-month old *Awat2*$^{-/-}$ (lower left panel) and 5-month old WT (lower right panel) mice stained with H&E *Awat2*$^{-/-}$ mice show patches of the thickened epidermis (*) and dilation of hair follicles (arrowhead) from the early age. C, Photograph of 14-month old *Awat2*$^{-/-}$ ear with skin lesions (top). Paraffin sections of affected ear stained with H&E showed thickening of epidermis (*) and hyperkeratosis (arrowhead) (bottom). D, Photograph of patches of fur loss affecting the dorsal side of 4-month old *Awat2*$^{-/-}$ mice. E, Loose and easily removable fur in 4-month old *Awat2*$^{-/-}$ mice (left), skin exposed after pulling off loose fur in *Awat2*$^{-/-}$ mice (middle), skin of shaved fur WT mice (right). F, Paraffin sections of skin of 14-month old *Awat2*$^{-/-}$ (left) and WT (right) mice stained with H&E *Awat2*$^{-/-}$ mice revealed smaller sebum-filled SGs (arrowhead) surrounding the hair follicle (top panel) and reduced number of SGs (white dashes outline) (lower panel) as compared to WT mice. Scale bars correspond to 0.5 mm in panels B, 1 mm in C-E, and 0.1 mm for panel F